



# Photoelectrochemical and photocatalytic properties of Fe@ZnSQDs/TiO<sub>2</sub> nanocomposites for degradation of different chromophoric organic pollutants in aqueous suspension

Mohtaram Danish<sup>1</sup> · M. Qamar<sup>2</sup> · MH Suliman<sup>2</sup> · M. Muneer<sup>1</sup>

Received: 16 June 2020 / Revised: 17 September 2020 / Accepted: 21 October 2020 / Published online: 3 November 2020  
© Springer Nature Switzerland AG 2020

## Abstract

Herein, synthesis of a novel nanocomposite comprising titania, iron, and zinc sulfide quantum dots (Fe@ZnSQDs/TiO<sub>2</sub>) is demonstrated, and its photoelectrochemical and photocatalytic properties are investigated. The photocatalytic performance is evaluated by studying the degradation of two organic pollutants, Rhodamine B and paracetamol, under both UV and visible light, while photoelectrochemical activity is determined by following water oxidation reaction. The findings indicate that the catalytic performance of ZnSQDs substantially improves after doping with Fe and fabricating heterostructure with TiO<sub>2</sub> nanoparticles, both under UV and visible radiations. The order of photocatalytic performance is discerned to be Fe@ZnSQDs/TiO<sub>2</sub> > TiO<sub>2</sub> > Fe@ZnSQDs > ZnSQDs, while photoelectrochemical is Fe@ZnSQDs/TiO<sub>2</sub> > Fe@ZnSQDs > ZnSQDs > TiO<sub>2</sub>. The variation in performance is correlated to electrochemical impedance, optical properties, generation of hydroxyl and superoxide radicals, and transportation of exciton. A mechanism is proposed highlighting the possible charge transfer reaction.

**Keywords** Fe@ZnSQDs/TiO<sub>2</sub> nanocomposite · UV and visible light active catalyst · Photocatalytic and photoelectrochemical study · Degradation of dye and paracetamol

## 1 Introduction

Wastes in water from different ventures and production lines are serious issues around the world. The release of wastes from dye industries is harmful to microorganisms, amphibian life, and a human being [1]. For the last few decades, photocatalytic degradation has been a consideration as an elective technique for the degradation of these effluents. Titanium dioxide (TiO<sub>2</sub>) was found to be one of the most effectual semiconductors in the degradation of organic and inorganic components present in water and air [2]. In addition,

semiconductor quantum dots (SQDs) have turned out to be well known due to their amazing electrical and optical properties. They display quantum confinement effect and have long fluorescence lifetime, narrow emission, and high quantum yield, which made them reasonable for applications, like light-producing diodes, bioanalysis, and luminescent sun-oriented concentrator [3]. Quantum dots (QDs) are a pristine class of luminous nanoprobe, having three measurements bound to 2–10 nm length scale [4]. The semiconducting material such as zinc sulfide (ZnS) has been impressively contemplated because of its wide band hole (nearly 3.68 eV for cubic phase ZnS, at room temperature), showing brilliant optical and electronic performance [5, 6]. Metal-doping of semiconductor materials is a fundamental and successful procedure for improving the optical, structural, morphological, magnetic, luminescent, and photocatalytic properties, to stretch out their relevance to different fields. Specifically, the doping of transition/rare earth particles into the ZnS upgrades the optical absorption, which impacts the bandgap, making it appropriate for photocatalytic devices [7]. Recently, transition metal ion (Cu, Fe, Ni, Co, Cr, etc.) doped semiconductors (ZnS, ZnO, CdS, ZnSe) have gained much attention [8]. Meanwhile, ZnS is a reasonable using host material for a huge

**Supplementary Information** The online version contains supplementary material available at <https://doi.org/10.1007/s42114-020-00187-9>.

✉ M. Muneer  
readermuneer@gmail.com; m.muneer.ch@amu.ac.in

<sup>1</sup> Department of Chemistry, Aligarh Muslim University, Aligarh 202002, India

<sup>2</sup> Centre of Excellence in Nanotechnology (CENT), King Fahd University of Petroleum & Minerals (KFUPM), Dhahran, Kingdom of Saudi Arabia

assortment of dopant because of the impacts of doping materials on the optical properties of QD semiconductors [9]. For example, the impact of iron dopant in the ZnS nanoparticles showed redshift as a key absorption edge with increasing iron concentration [10]. In spite of the fact of being a wideband hole semiconductor, ZnS nanoparticles can likewise be related to TiO<sub>2</sub> to expand its photocatalytic action due to high potentials of valence band h<sup>+</sup> and conduction band e<sup>-</sup> (+ 1.85 and - 1.75 V versus hydrogen electrode) [11, 12]. Recently, considerable progress in the synthesis and study of doped ZnSQDs with various semiconducting materials such as TiO<sub>2</sub>, SnO<sub>2</sub>, CuS, g-C<sub>3</sub>N<sub>4</sub>, and ZnO has been made [13–16]. For instance, Houcine and coworkers synthesized composite of ZnSQDs with TiO<sub>2</sub> in aqueous solution using 3-mercaptopropionic acid to determine the photodegradation efficiency of salicylic acid [16]. Franco and coworkers demonstrated a general strategy for distinct nanocrystalline TiO<sub>2</sub> capped ZnS samples through the chemical deposition method [17].

As a part of this work, we have built up a quick and proficient method for the expulsion of contamination into dye (for example, Rhodamine) and pharmaceutical drug like paracetamol (acetaminophen, 4-acetamidophenol, N-acetyl-4-aminophenol, 4-hydroxyacetanilide, APAP) constructed on photocatalytic action of semiconductor nanoparticles (for example, quantum dots). Herewith, we make a report for the synthesis of a nanocomposite (Fe@ZnS QDs/TiO<sub>2</sub>), followed by their characterization and photocatalytic testing by studying the affective degradation of a dye (Rhodamine B (RhB)) and a drug derivative (paracetamol). In addition, the mineralization of paracetamol (measured in terms of depletion in TOC content) was also investigated because, in many cases, these reactions generate more toxic intermediates during the photooxidation process. In continuation of our studies, the photoelectrochemical performance of as-prepared photocatalysts towards water oxidation was also investigated in a three-electrode quartz cell assembly.

## 2 Experimental section

### 2.1 Materials

Zinc acetate dihydrate (Zn (CH<sub>3</sub>COO)<sub>2</sub>·2H<sub>2</sub>O), dye derivative Rhodamine B (RhB), and paracetamol (PCM) were obtained from Sigma Aldrich, whereas sodium sulfide (Na<sub>2</sub>S) and iron (Fe (NO<sub>3</sub>)<sub>3</sub>·9H<sub>2</sub>O) were purchased from Merck. The other chemicals used in this study, such as terephthalic acid (TA), isopropyl alcohol (IPA), and benzoquinone, were obtained from Merck. Degussa P25 TiO<sub>2</sub> sample was obtained as a gift sample from Evonik Pvt. Ltd., Bombay, India. Water used in all experiments was double distilled (DDW).

### 2.2 Synthesis of pure and Fe-doped ZnSQDs

The zinc sulfide quantum dot (ZnSQD) nanoparticles were synthesized by a chemical precipitation method according to the procedure reported in the literature [18], and Fe-doped ZnSQD samples were synthesized by a similar procedure. In a typical synthesis, Zn(CH<sub>3</sub>COO)<sub>2</sub>·2H<sub>2</sub>O (1.94 M and 1.88 M) and Fe(NO<sub>3</sub>)<sub>3</sub>·9H<sub>2</sub>O (0.06 M and 0.12 M) were mixed in the molar ratio (Zn:Fe = 0.97:0.03 and 0.93:0.06) in water (50 mL) in a RB flask and stirred for 30 min. A 2 M aqueous sodium sulfide solution was added dropwise under stirring. The content was heated at 80 °C under constant stirring for 2 h. The obtained precipitate was separated through centrifugation and washed with twofold distilled water and ethanol. The precipitate was dried at 120 °C for 10 h and grounded to a fine powder to acquire 3% and 6% Fe@ZnSQDs.

### 2.3 Preparation of Fe@ZnSQDs/TiO<sub>2</sub> nanocatalyst

In a typical experiment, 0.95 g of TiO<sub>2</sub> was put off into 50 mL of methanol, followed by sonication for 30 min. Thereafter, 5 wt% of synthesized Fe@ZnSQDs was added to the above mixture and stirred for 24 h. The as-obtained precipitate was filtered and washed away with ethanol and water and dried at 120 °C 6 h, which was grounded and characterized using standard techniques.

### 2.4 Material characterization

The phase structure of synthesized nanoparticles was determined using an X-ray diffractometer (Shimadzu XRD model 6100) utilizing graphite monochromatic copper radiation (Cu K $\alpha$  radiation (1.540 Å) which is operated at 30 kV voltage and 15 mA current in the 2 $\theta$  territory 5–80° at the output speed of 10.0° per minute. The morphology of the synthesized samples was determined using FESEM analysis, performed with TESCAN MIRA 3 LMU. FTIR spectra were recorded in KBr material using Perkin Elmer Spectrum 2 model. UV–Vis diffuse reflectance spectra (DRS) were used for the measurement of the optical properties of the synthesized material with a Perkin Elmer Lambda 35 UV–Vis spectrophotometer. The surface chemical state and elemental position of the samples were recorded on an X-ray photoelectron spectroscopy (XPS–Leybold Heraeus) using 30 W Al K $\alpha$  radiation. Photoluminescence spectra were measured by a fluorescence spectrometer (Perkin Elmer LS 55). PEC measurements were carried out utilizing potentiostat/galvanostat–Princeton Applied Research (273A) and light source–Asahi Spectra (MAX-303).

## 2.5 Evaluation of photocatalytic activity

A photochemical reactor comprising of Pyrex glass was used throughout all photolysis experiments. Rhodamine B (RhB) and paracetamol in aqueous suspension were used as a pollutant to check the photocatalytic performance of the synthesized materials under the air atmosphere. A 500-W tungsten halogen bulb was used as a visible light source, and a 125-W medium pressure mercury lamp discharging wavelength in the range of 300–400 nm was utilized as ultraviolet light (UVA) source. The light force was estimated with a UV light detector (Lutron UV-340), in the range between 1.49 and 1.51 mW/cm<sup>2</sup>. The temperature of the arrangement was kept up underneath 25 °C by providing moderate water throughout the experiments. A simplified schematic diagram representation of the photochemical reaction vessel is shown in our previous report [19], which is used in this experiment. In a typical experiment, an aqueous solution of compound (220 mL, 10 ppm) was taken in the reactor and the catalyst (1 g L<sup>-1</sup>) was put off and sonicated for 15 min to ensure the adsorption-desorption equilibrium and then, it was stirred and purged with air through the experiment. At different time intervals, 5 mL sample was collected and centrifuged to remove the catalyst and analyzed. The degradation of the compound under investigation was observed by measuring the variation in absorbance at their  $\lambda_{\max}$  ( $\lambda_{\max}$  = 553 nm (Rhodamine B),  $\lambda_{\max}$  = 243 nm (paracetamol)) as a function of time using a UV–Vis spectrophotometer (Perkin Elmer Lambda 35).

The degradation proficiency (DP) of the catalysts was evaluated by using the following expression:

$$DP (\%) = (C_0 - C_t) / C_0 \times 100 \quad (1)$$

where  $C_0$  and  $C_t$  are the initial concentration of pollutants after the adsorption-desorption equilibrium process and final concentration of the above toxins at various light times, respectively. To assess the mineralization proficiency of catalysts, total organic carbon (TOC) content of paracetamol was measured using the Shimadzu TOC-V<sub>CSH</sub> model. The high-performance liquid chromatography (HPLC) method with UV–Vis photodiode array detector model 2489, WATERS binary HPLC pump model 515, and Symmetry C18 (75 \* 4.6 mm) column was used and the detector was set at 254 nm throughout the experiment. A linear gradient elution (methanol:water) was used to reach 60% methanol:40% water (60:40 v/v) mobile phase with an injection volume of 20  $\mu$ L.

## 2.6 Determination of active species

Trapping analysis was conducted to assess the involvement of active species in the degradation of pollutants by using different scavengers into the solution of individual pollutants such as RhB and paracetamol under the same conditions as in the

photocatalytic activity portion. In this experiment, equal molar concentration (3 mM) of scavengers such as isopropyl alcohol to trap the generated  $\cdot$ OH radicals, BQ to trap the superoxide radicals [20, 21], and EDTA-2Na was used to trap hole in the solution by providing electrons [22, 23]. The terephthalic acid (TA) photoluminescence probe method was adopted to determine the number of hydroxyl radicals produced during the photocatalysis process. In a typical method, 220 mg of catalyst (Fe@ZnSQDs/TiO<sub>2</sub>) was suspended in an aqueous solution of 220 mL of TA (0.5 mM) in aqueous NaOH (2 mM) solution. All the reaction circumstances were alike to those used for the photocatalytic activity only with the change of the solution of terephthalic acid by the solution of a pollutant, as mentioned in our previous reports [24, 25]. At certain time breaks, generated hydroxyl radicals were enumerated by PL spectrophotometer at an excitation wavelength of 315 nm. The signal detected at 425 nm relates to the production of hydroxyl radicals.

## 3 Results and discussion

### 3.1 XRD analysis

To explore the purity and crystalline structure of nanoparticles, X-ray diffractometry was performed on differently prepared samples. The XRD spectra of pure TiO<sub>2</sub>, ZnSQDs, Fe@ZnSQDs, and Fe@ZnSQDs/TiO<sub>2</sub> composites are shown in Fig. 1. The crystal structure of the bottom three examples with peaks indexed as (1 1 1), (2 2 0), and (3 1 1) is cubic zinc blend, which matches well with the standard card JCPDS NO. 5-566. The expansion of dopant alters the peak position and intensity. The width of the peaks is due to the small size of the crystals. In the XRD patterns of TiO<sub>2</sub> and Fe@ZnS QDs/TiO<sub>2</sub>, the peaks at an angle of  $2\theta = 25.1^\circ$ ,  $37.8^\circ$ ,  $48^\circ$ ,  $54.2^\circ$ ,  $55.2^\circ$ ,  $62.8^\circ$ ,  $68.9^\circ$ ,  $70.7^\circ$ , and  $75^\circ$  are connected to the diffraction from the (101), (004), (200), (105), (211), (204), (116),

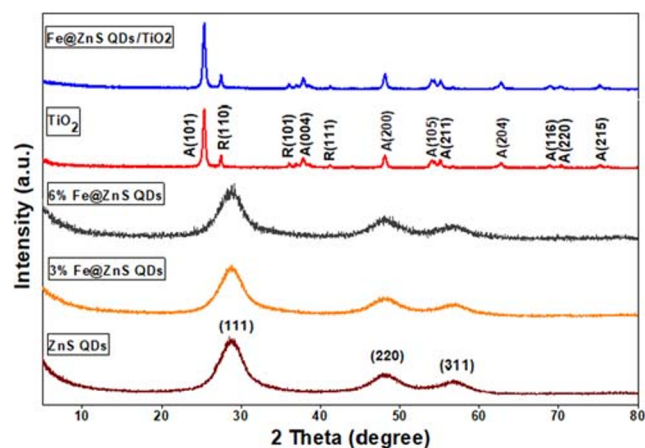


**Fig. 1** XRD patterns of ZnSQDs, Fe@ZnSQDs (3% and 6%), pure TiO<sub>2</sub>, and Fe@ZnS QDs/TiO<sub>2</sub>

(220), and (215) TiO<sub>2</sub> anatase phase crystal plane, respectively, and the peaks at  $2\theta = 27.4^\circ$ ,  $36.2^\circ$ , and  $41.2^\circ$  are due to the diffraction from the (110), (101), and (111) TiO<sub>2</sub> rutile phase crystal planes [19]. In light of the low substance of Fe@ZnSQDs in the TiO<sub>2</sub> sample, the XRD pattern of this sample could not differentiate these peaks. After the formulation of Fe@ZnSQD-loaded TiO<sub>2</sub> nanocomposite, the crystal structure and anatase to rutile ratio of TiO<sub>2</sub> were conserved. The presence of Fe@ZnSQDs does not interfere with the TiO<sub>2</sub> crystal structure in this way. No diffraction peaks were detected from impurities in all of the samples. The average particle size (shown in Table S1) of the different synthesized materials was calculated from the XRD data, using the Scherrer formula (Eq. 2) [26].

$$D = K\lambda/\beta \cos\theta \quad (2)$$

where  $D$ ,  $\lambda$ ,  $K$ , and  $\beta$  are the crystallite size (nm), the wavelength of X-beam radiation (0.15418 nm), Scherrer constant (0.94), and FWHM (full-width half-maximum), respectively. The crystallite sizes of doped and undoped ZnSQDs were found to be in the range of 2.4 to 2.47 nm (shown in Table S1), which are altogether smaller than the excitonic Bohr radius of ZnS (~2.5 nm) [18].

### 3.2 FTIR analysis

To better understand the structure of the surface of all the synthesized materials, FTIR analysis was carried out. The FTIR spectrum of pure TiO<sub>2</sub>, ZnSQDs, Fe@ZnSQDs, and Fe@ZnSQDs/TiO<sub>2</sub> composite is shown in Fig. S2. The broadband at 500–600 cm<sup>-1</sup> (TiO<sub>2</sub> and Fe@ZnSQDs/TiO<sub>2</sub>) could be assigned to the vibration of the Ti–O bonds [27]. ZnSQDs and Fe@ZnSQDs show a strong peak at 649 cm<sup>-1</sup>, which could be ascribed to the Zn–S (metal sulfide) bond [28]. The other strong peak in all materials at 3400 cm<sup>-1</sup> reveals the presence of –OH stretching frequency (existence of water absorbed on the surface of catalysts). However, the FTIR spectrum of Fe@ZnSQDs indicates almost similar peaks concerning the undoped ZnSQDs, and moreover, a recognizable new peak at 1120 cm<sup>-1</sup> might be because of the distinction in vibrational modes of Zn and (Fe) sulfide ions. This indicates the fractional Fe substitution of Zn ions as Fe–S–Zn. The results all together confirm the presence of Fe@ZnSQDs into TiO<sub>2</sub>.

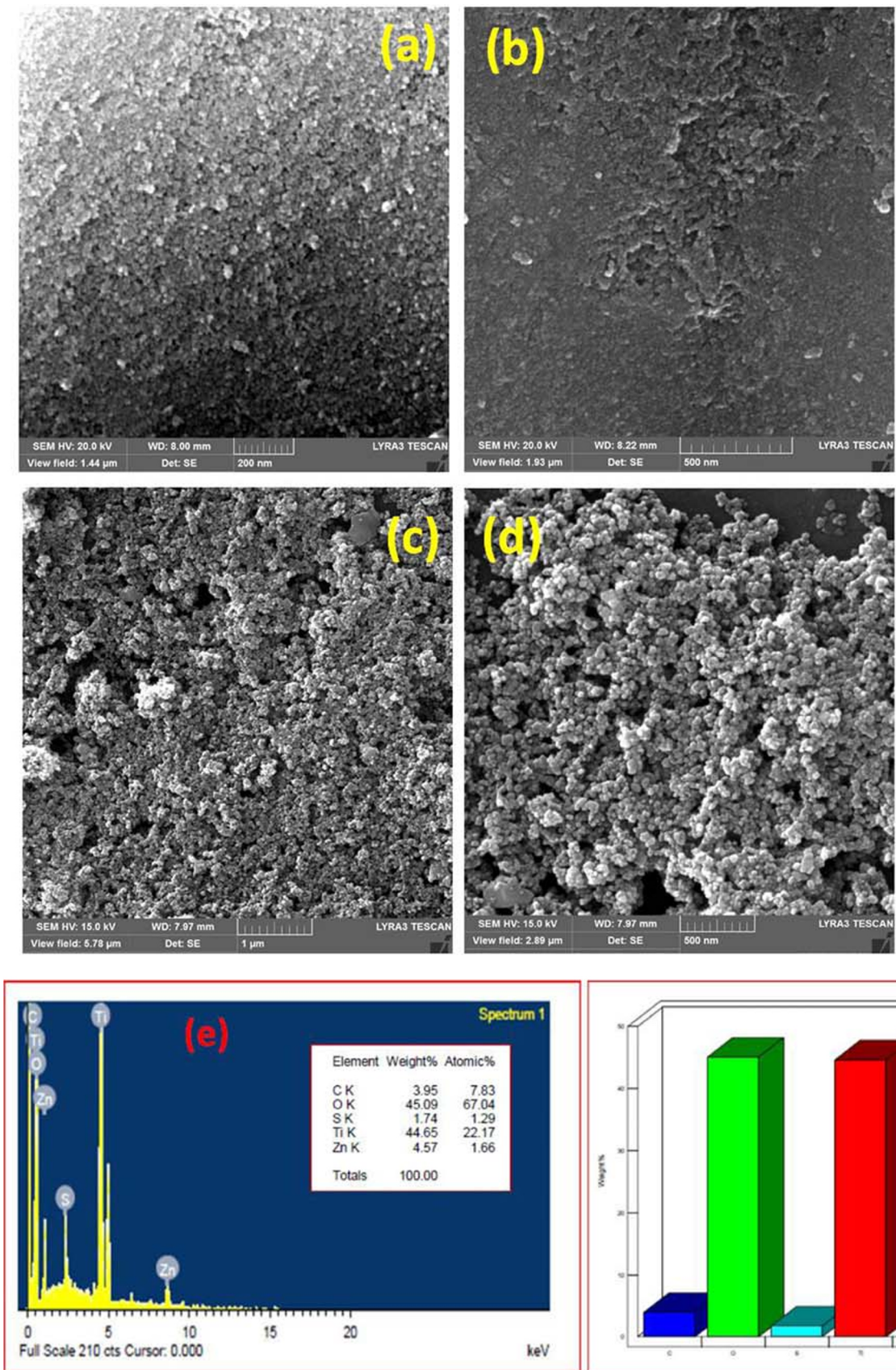
### 3.3 SEM analyses

Figure 2a–d show the FESEM images of ZnSQDs, Fe@ZnSQDs, and Fe@ZnSQDs/TiO<sub>2</sub>. Figure 2a shows the SEM image of ZnSQDs, indicating a spherical-shaped particle

with a size of approx.  $2.57 \pm 0.5$  nm (confirmed by XRD). The particles are agglomerated due to the larger surface area of quantum dots. It is clearly observed that the agglomeration level is altered in the Fe@ZnSQDs compared to the undoped sample (Fig. 2b). Thus, Fe doping has little influence on the particle size and surface morphology of ZnSQDs, showing the non-uniform distribution of particles. A high-resolution SEM image (Fig. 2d) shows no significant changes in the morphology of Fe@ZnSQDs/TiO<sub>2</sub> on the deposition of Fe@ZnSQDs onto the surface of TiO<sub>2</sub>, indicating the very small size of the ZnSQDs. The presence of Fe@ZnSQDs on the TiO<sub>2</sub> in Fe@ZnSQDs/TiO<sub>2</sub> was additionally confirmed by XPS analysis, as shown in Fig. 3. The EDX spectra and wt% of each element present in Fe@ZnSQDs/TiO<sub>2</sub> nanocomposite are shown in Fig. 2e and f, which indicate that all of the elements are present in the composite material and also the compositions of all elements were found to be nearly close to those of the wt% of the different metals. The element “Fe” is not detected in EDS spectra which might be due to the low content of Fe@ZnSQDs in the composite material, which was further confirmed by the XPS analysis, as shown in Fig. 3.

### 3.4 XPS analysis

XPS technique was utilized to evaluate the surface composition and the chemical state of the Fe@ZnSQDs/TiO<sub>2</sub> nanoparticle. The outcomes of the review output and high-resolution XPS spectra are shown in Fig. 3. Figure 3a shows the survey scan of Fe@ZnSQDs/TiO<sub>2</sub> nanoparticles, which confirmed the presence of all elements such as Ti, Zn, Fe, O, and S in the material. The high-resolution XPS study of the individual elements shown in Fig. 3b–f indicate that Zn, Ti, Fe, O, and S are existing at their corresponding binding energy. Figure 3b demonstrates the high-resolution spectrum of Zn and two peaks at a binding energy of 1022.17 and 1045.24 eV which could be attributed to Zn 2p<sub>3/2</sub> and Zn 2p<sub>1/2</sub>, respectively [29]. Zn exists in the form of Zn<sup>2+</sup> in ZnSQD nanoparticles which was confirmed by the energy difference between two peaks, which was found to be 23.07 eV [30]. In Fig. 3c, Ti 2p<sub>1/2</sub> and Ti 2p<sub>3/2</sub> spin-orbit states at approximately 464.54 eV and 458.76 eV, respectively, show the binding energies of the Ti core levels, which in turn exhibits the existence of +4 oxidation state of Ti in TiO<sub>2</sub> [31, 32]. Figure 3d demonstrates two weak signals of Fe 2p identified at 710.64 and 724.43 eV, which was allocated to Fe 2p<sub>3/2</sub> and Fe 2p<sub>1/2</sub>, respectively [33]. A sharp peak in O 1s XPS signal at binding energy 530.03 eV is ascribed to the –2 oxidation state of oxygen [34]. In addition, a peak at the binding energy of 168.93 eV indicates that the S exists as S<sup>2-</sup> in S 2p spectrum [35], as shown in Fig. 3e. From the



**Fig. 2** FESEM image of ZnSQDs (a), and Fe@ZnSQDs (b), low- and high-resolution images of Fe@ZnSQDs/TiO<sub>2</sub> (c, d), EDX spectra of Fe@ZnSQDs/TiO<sub>2</sub> (e), and wt% of existing elements (f)

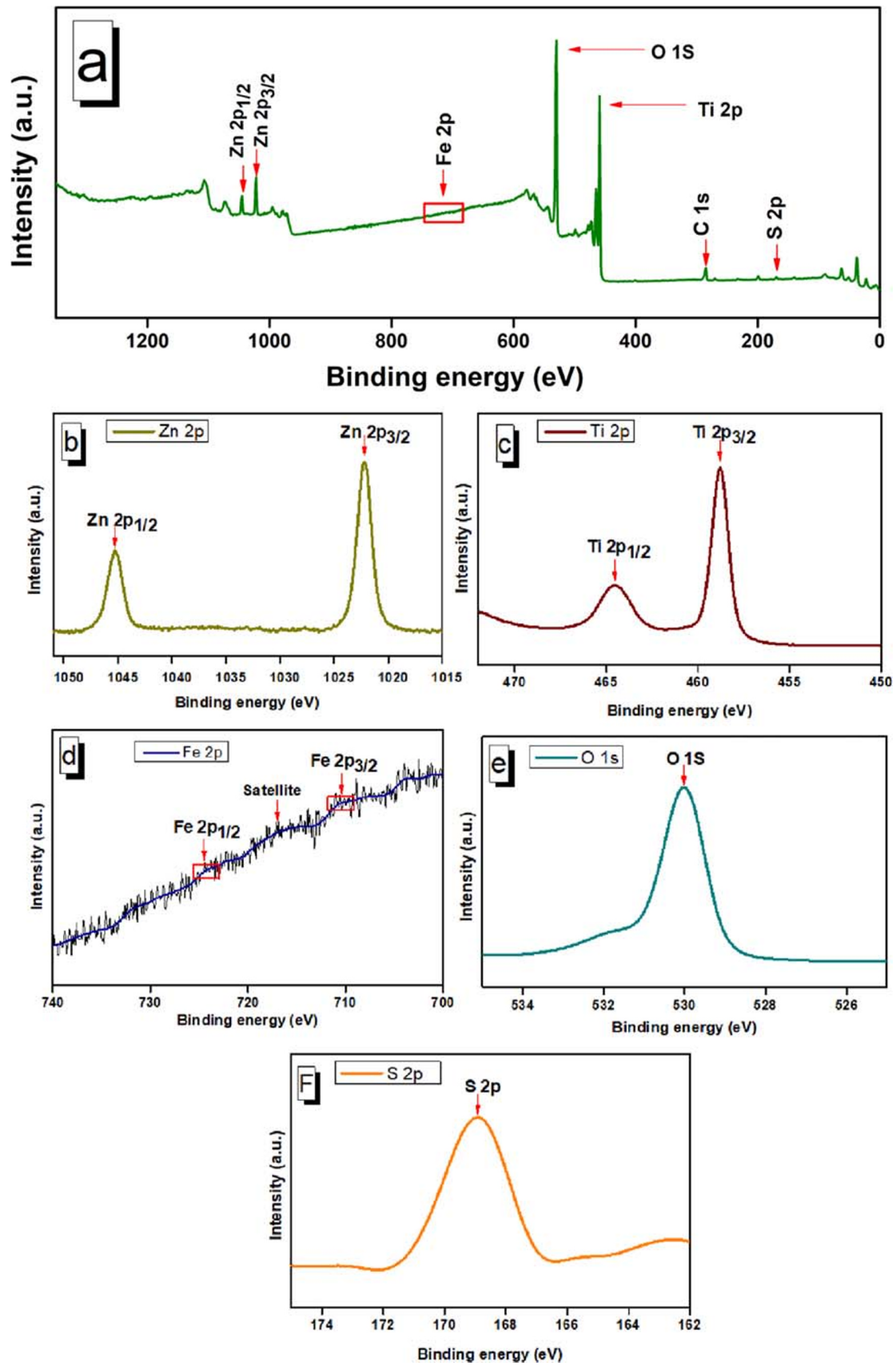


Fig. 3 XPS study scan spectrum of the synthesized Fe@ZnSQDs/TiO<sub>2</sub> (a); high-resolution XPS spectra of Zn 2p (b), Ti 2p (c), Fe 2p (d), O 1s (e), and S 2p (f)

XPS results, we could conclude that Fe@ZnSQDs/TiO<sub>2</sub> nanocomposite was effectively synthesized.

### 3.5 UV–Vis DRS analysis

The optical properties of the synthesized materials were investigated by executing UV–Vis DRS analysis from 200 to 700 nm and the results have been shown in Fig. 4a. From the figure, it was easy to see that bare ZnSQD demonstrates an absorption edge at 344 nm with wide bandgap energy, implying that ZnSQDs may be activated only under UV light illumination. On doping with Fe, Fe@ZnSQD nanoparticles detected a slight shift towards higher wavelength. The doping of Fe generates a new state beneath the CB of ZnSQDs, which may lower the separation between the bandgap and consequently allowing more absorption of light at a higher wavelength. The results also indicate that 6% Fe@ZnSQD sample demonstrates a strong absorption towards higher wavelength as compared with the pure ZnSQDs and 3% Fe@ZnSQDs, which may, in turn, result in the significant improvement in photocatalytic action of Fe@ZnSQDs/TiO<sub>2</sub> composite materials.

The bandgap energies of the prepared samples were calculated by the following equation:

$$(\alpha h\nu) = A(h\nu - E_g)^{n/2} \quad (3)$$

where  $\alpha$  is an absorption coefficient,  $\nu$  is the light frequency,  $E_g$  is the bandgap, and  $A$  is a constant. The value of  $n$  could rely on the sort of electronic change; for example,  $n = 1$  and  $n = 4$  are for direct and indirect transition, respectively.

Figure 4 b shows a plot of  $(\alpha h\nu)^2$  versus  $h\nu$ . The  $E_g$  values for nanoparticles were resolved to utilize extrapolating the straight line of the curve on  $h\nu$  axis; the bandgap energies of pure ZnSQDs and Fe@ZnSQDs/TiO<sub>2</sub> composite were found to be from 3.60 to 3.34 eV, as shown in Fig. 4b. The bandgap energy evaluated results demonstrate that the prepared composite material could perform proficiently high photocatalytic activity under UV light illumination. On doping with Fe, we see a shift towards higher wavelength; therefore, we additionally tested the photocatalytic action of composite materials under the visible region as well.

### 3.6 Photoluminescence study

Photoluminescence (PL) spectroscopy was utilized to examine the energized conditions of semiconductors, since photocatalytic action is associated with lifetime and catching of electron and hole pairs. On illumination of semiconducting material, the recombination of  $e^-/h^+$  produces the emission of photons leading to photoluminescence. It is outstanding that the PL intensity is legitimately identified with the recombination rate of the electron-hole pair. For the most part, more fragile PL response leads to a slow recombination rate, subsequently increasing the lifetime of photogenerated charge carriers and, consequently, better photocatalytic activity [36]. Figure S3 shows the PL spectra of different catalysts such as TiO<sub>2</sub>, ZnSQDs, Fe@ZnSQDs, and Fe@ZnSQDs/TiO<sub>2</sub> at an excitation wavelength of 320 nm. As shown in the figure, PL spectra of ZnSQDs and Fe@ZnSQDs were found to be less intense than of TiO<sub>2</sub> and least with Fe@ZnSQDs/TiO<sub>2</sub>. The results clearly indicate that the electron-hole pair

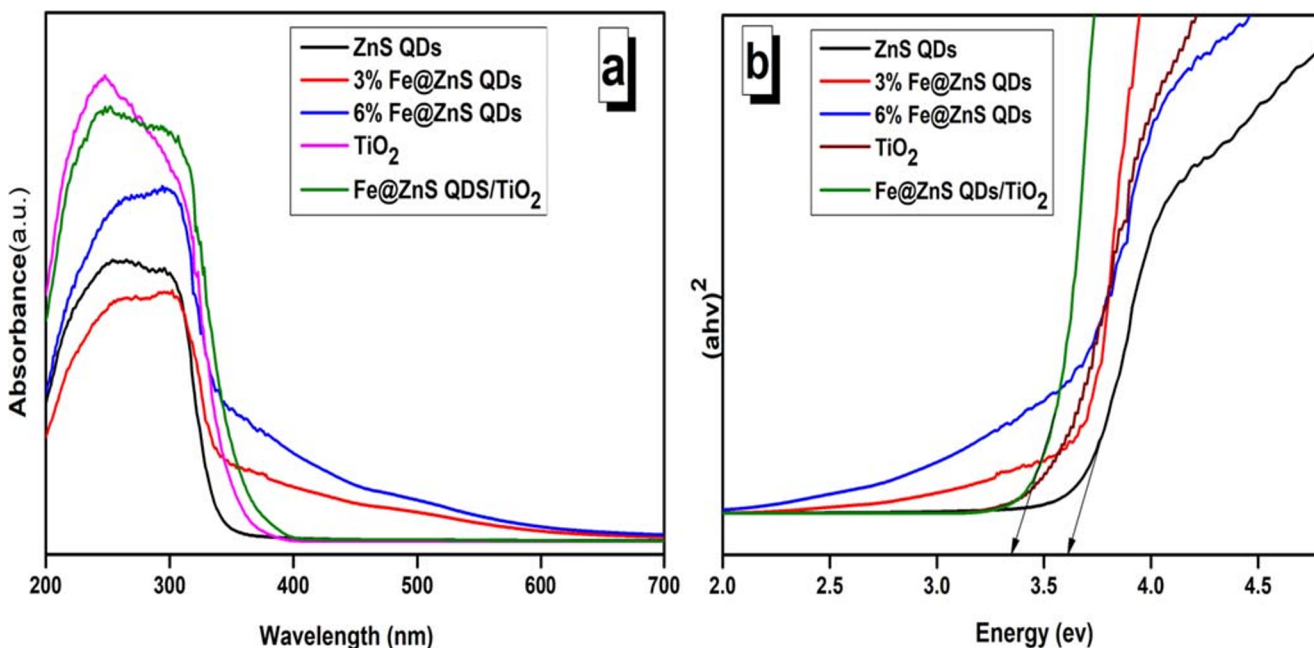


Fig. 4 a UV–Vis DRS spectra of different materials, and b their corresponding Tauc's plot

recombination has been found to be minimized for Fe metal-doped nanoparticle, prompting the better separation of photo-produced charge carriers, which can eventually benefit the photocatalytic action of the materials.

### 3.7 Photocatalytic degradation study

The photocatalytic action of the different synthesized photocatalysts such as ZnSQDs with various mole % of Fe and Fe@ZnSQDs/TiO<sub>2</sub> composite were assessed by studying the degradation of RhB and paracetamol in aqueous suspension under UV-light as well as Vis-light source in the presence of atmospheric oxygen. It is assumed that the adsorption of pollutants on the photocatalyst surface is a prerequisite in the photocatalytic degradation of organic pollutants [24]. Therefore, all photochemical tests were done under adsorption-desorption equilibration by stirring the aqueous solution of the compound in the presence of a photocatalyst for 25–30 min under a dark environment. The time-dependent UV–Vis absorption spectra of irradiation of an aqueous solution of RhB and paracetamol in the presence of Fe@ZnSQDs/TiO<sub>2</sub> composite under visible light are shown in Fig. 5a and b. As seen in the figure, the absorption intensity decreases with increasing illumination time and about 94% and 88% of degradation was observed for RhB and paracetamol, respectively, during 75 min of irradiation. The concentration of dye derivatives/paracetamol was determined through the standard calibration curve obtained from the absorbance of dye/paracetamol at various concentrations. Figure 6a and b show the variation in concentration of RhB and paracetamol versus irradiation time in the absence and presence of various photocatalysts like ZnSQDs, TiO<sub>2</sub>, Fe@ZnSQDs, and Fe@ZnSQDs/TiO<sub>2</sub> composites. It could be seen that the degradation of RhB and paracetamol is insignificant in the absence of

catalysts, demonstrating that these compounds are quite stable and could not be degraded under direct photolysis. It could also be seen that both compounds were found to be degraded more efficiently in the existence of Fe@ZnSQDs/TiO<sub>2</sub> as compared to other doped and undoped samples. The degradation rate of pollutants with various photocatalysts was found to be in the order Fe@ZnSQDs/TiO<sub>2</sub> > TiO<sub>2</sub> > Fe@ZnSQDs > ZnSQDs.

The photodegradation of both compounds was also investigated using a synthesized catalyst under analogous conditions using a UV-light source. The time-dependent UV–Vis absorption spectra of irradiation of an aqueous solution of RhB and paracetamol in the presence of Fe@ZnSQDs/TiO<sub>2</sub> composite under UV light are shown in Fig. S4 a and b. It was seen that decreases in the absorption intensity with increasing irradiation time and about 95% and 74% degradation of RhB and paracetamol were observed within 10 min under a similar condition. The better efficiency of Fe@ZnSQDs/TiO<sub>2</sub> for the degradation of both compounds under UV light could be attributed to better UV-light absorbing ability and efficient charge carrier separation (due to the generation of heterojunction between ZnSQDs and TiO<sub>2</sub> in the composite material). Figure S5 represents the change in concentration versus illumination time with and without using photocatalysts for the degradation of both compounds under UV-light source. The results clearly indicate the superb activity of synthesized materials for the degradation of RhB and paracetamol under both visible and UV light illumination. These reactions lead to the formation of some by-products, and accordingly, complete mineralization is desirable. Henceforth, the photo-mineralization of organic compounds was investigated by contemplating the removal of TOC content as a function of time by irradiation of an aqueous suspension of model pollutants in the presence of a catalyst under similar conditions. Figure S6 shows the change in TOC content in a periodic time interval by

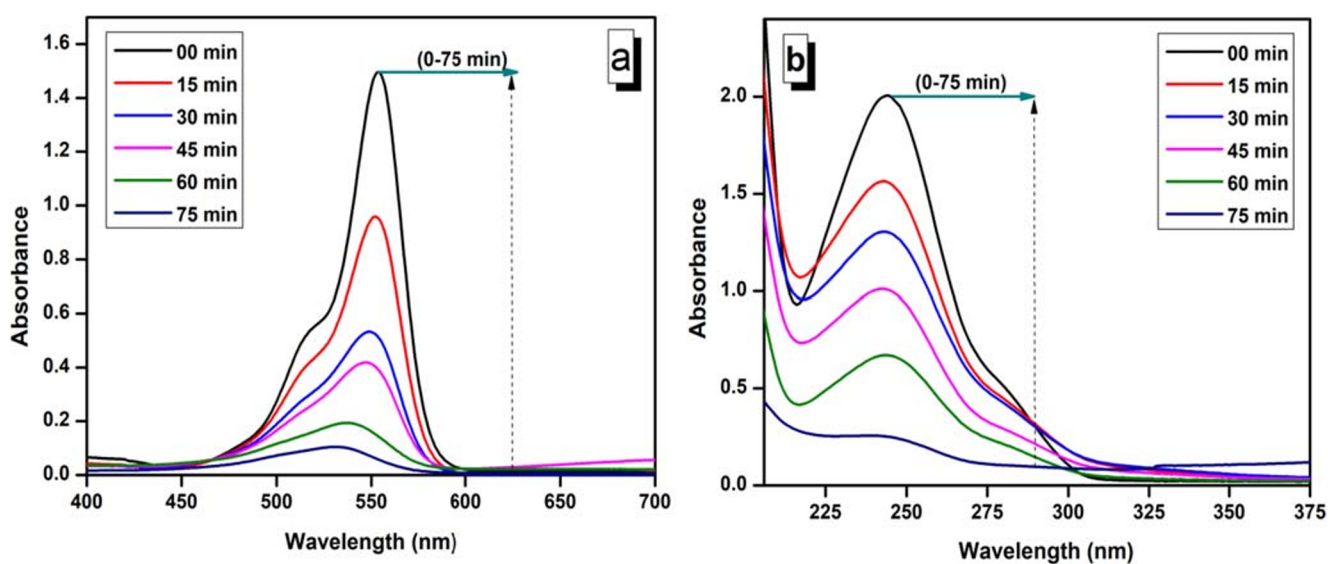


Fig. 5 Change in absorbance of RhB (a) and paracetamol (b) in the presence of Fe@ZnSQDs/TiO<sub>2</sub> at different time intervals under visible light illumination



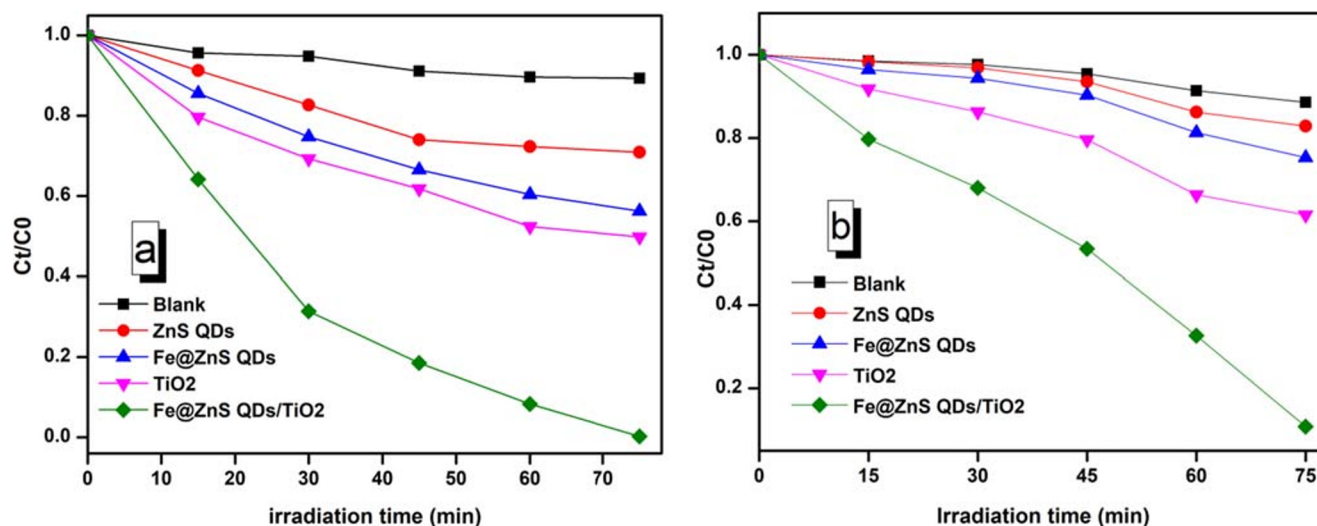


Fig. 6 Change in concentration of RhB (a) and paracetamol (b) as a function of time in the presence of different catalysts under visible light illumination

irradiation of an aqueous suspension of paracetamol in the presence of the best one photocatalyst (Fe@ZnSQDs/TiO<sub>2</sub>) under UV-light source and atmospheric oxygen. It could be seen from the figure that 61% of mineralization was found in 40 min of illumination, showing the strong photocatalytic ability of the synthesized material. The results indicate that Fe@ZnSQDs/TiO<sub>2</sub> not only degrades the paracetamol but also mineralizes the toxic organic carbon into inorganic components.

### 3.8 HPLC measurement

The photocatalytic activity of the synthesized catalyst, Fe@ZnSQDs/TiO<sub>2</sub>, for the degradation of paracetamol was also monitored using the HPLC analysis technique with an intention to look into the by-products formed in between the photooxidation process. Figure S7 shows the HPLC of the irradiated mixture at various time breaks on irradiation of paracetamol in the presence of Fe@ZnSQDs/TiO<sub>2</sub> composite nanoparticles under UV light. The figure clearly indicates that peak appearing at a retention time ( $R_t$ ) of 0.8 mins gradually decreases with increasing irradiation time, indicating 74% degradation in 75 min of illumination.

### 3.9 Evaluation of photoelectrochemical (PEC) activity

The photoelectrochemical performance of as-prepared photocatalysts towards water oxidation was investigated in a three-electrode quartz cell assembly. The measurements were carried out in a 0.1 M Na<sub>2</sub>SO<sub>4</sub> aqueous solution. The photoelectrodes (working electrode) were prepared as follows. A measured amount of photocatalysts (10 mg) was suspended in a solution of the water-ethanol mixture containing Nafion as a binder. The suspension was thoroughly homogenized by sonication. The resulting suspension was drop-casted on an FTO substrate. The loading of photocatalysts on FTO was 1 mg cm<sup>-2</sup>.

Saturated calomel electrode was used as the reference and coiled platinum wires as the counter electrodes.

The photocurrent (water oxidation) was recorded as a function of time, and the time-dependent current profiles are shown in Fig. 7, by switching the light on and off for 600 s at a continually applied potential of 0.75 V<sub>SCE</sub>. The increasing order of photocurrent is found to be in the order TiO<sub>2</sub> < ZnSQDs < Fe@ZnSQDs < TiO<sub>2</sub>/Fe@ZnSQDs. The highest photocurrent (approximately 0.12 mA cm<sup>-2</sup>) was recorded in the presence of Fe@ZnSQDs/TiO<sub>2</sub>, while the TiO<sub>2</sub> electrode produced the lowest photocurrent (0.02 mA cm<sup>-2</sup>). The current signal detected in the absence of light was negligible, suggesting the generated photocurrent is the result of photoexcitation.

In addition to optical properties (absorption and excitation), the charge transport capability of semiconducting materials has a significant impact on the photocatalytic performance. Electrochemical impedance spectroscopy (EIS), therefore, was employed to study electrical conductivity and surface charge transfer kinetics of the as-prepared photoelectrodes. The experiments were carried out in the frequency range between 10<sup>5</sup> Hz and 0.01 Hz at 0.75 V<sub>SCE</sub> in 0.1 M Na<sub>2</sub>SO<sub>4</sub> aqueous solution. The Nyquist plots (real vs. imaginary impedance) of TiO<sub>2</sub>, ZnSQDs, Fe@ZnSQDs, and Fe@ZnSQDs/TiO<sub>2</sub> were obtained under dark conditions and UV-Vis radiations. The experimental data were processed using the Randles equivalent circuit, which comprises solution resistance ( $R_s$ ) in sequence with a sub-circuit of charge transfer resistance ( $R_p$ ) in parallel with a capacitor ( $C_p$ ). The Nyquist plots of different photoelectrodes are compared in Fig. 8. In Nyquist plots, the radius of the semicircle directly relates to the resistance at the solid-liquid interface—the shorter the radius, the smaller the resistance and the faster the charge transfer between photocatalysts surface and water. Under dark conditions, ZnSQDs possess substantially lower electrical resistance (~37 kΩ) as compared to the TiO<sub>2</sub> electrode (~325 kΩ).

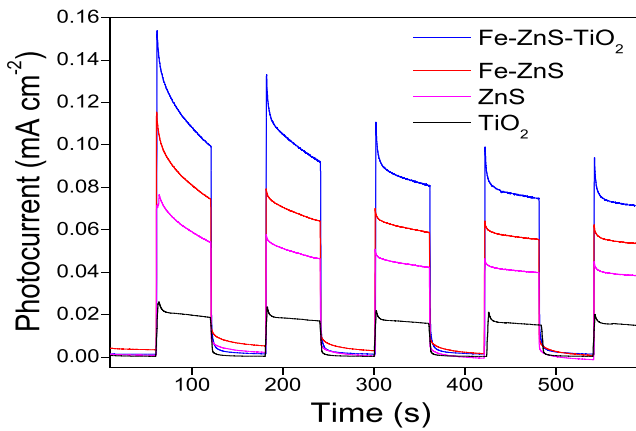


**Fig. 7** Comparative current of photoelectrodes recorded under intermittent light illumination:  $\lambda = 300\text{--}600\text{ nm}$ ,  $0.1\text{ M Na}_2\text{SO}_4$ ,  $V_{\text{SCE}} = 0.75\text{ V}$

The resistance of ZnSQDs was further decreased to be  $\sim 7\text{ k}\Omega$  upon Fe doping. The Fe@ZnSQDs/TiO<sub>2</sub> photoelectrode possessed significantly higher resistance ( $\sim 280\text{ k}\Omega$ ) than ZnSQDs and Fe@ZnSQDs, presumably due to the presence of TiO<sub>2</sub>. While the resistance of photoelectrodes decreases upon illumination, the trend of dark conditions was maintained and the decreasing order of electrical resistance was determined to be TiO<sub>2</sub> > Fe@ZnSQDs/TiO<sub>2</sub> > ZnSQDs > Fe@ZnSQDs. Better charge transport properties usually

translate into better charge separation and hence high performance.

### 3.10 Determination of reactive species involved in photodegradation

The trapping of dynamic species such as superoxide and hydroxyl radicals involved in the degradation course was assessed by contemplating the photodegradation of RhB-containing catalyst within sight of three distinct quenchers, such as isopropyl alcohol (IPA), benzoquinone (BQ), and disodium ethylenediaminetetraacetate (EDTA), under similar circumstances. Figure S8a demonstrates the trapping experiments on irradiation of an aqueous suspension of RhB with and without previously mentioned quenchers over Fe@ZnSQDs/TiO<sub>2</sub> under visible light irradiation. It is seen from the figure that all the quenchers under investigation reduce the degradation rate of RhB. On the addition of the BQ ( $\text{O}_2^-$  scavenger), the rate was found to inhibit maximum reducing the degradation rate from 94 to 51%, indicating superoxide radical anion being the main reactive species which take part in the photooxidation model compound in the presence of Fe@ZnSQDs/TiO<sub>2</sub> catalyst.

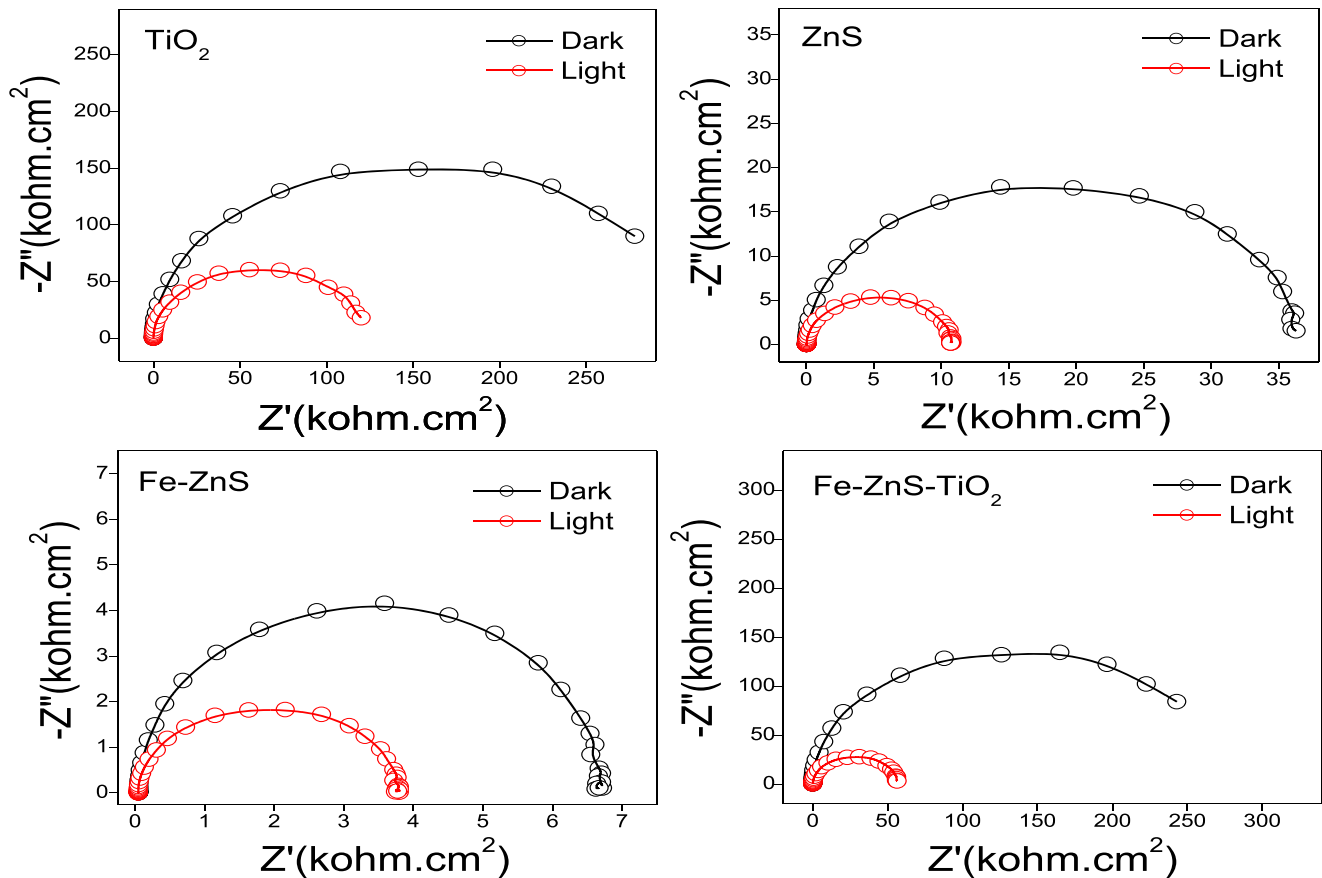
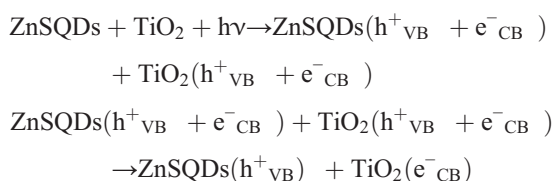


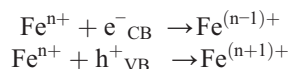
**Fig. 8** Comparative Nyquist plots of TiO<sub>2</sub>, ZnSQDs, Fe@ZnSQDs, and Fe@ZnSQDs/TiO<sub>2</sub> under dark and light conditions.  $\lambda = 300\text{--}600\text{ nm}$ ,  $V = 0.75\text{ V}_{\text{SCE}}$ ,  $0.1\text{ M Na}_2\text{SO}_4$

In addition, the terephthalic acid photoluminescence method (TA-PL) was also studied to investigate the role of  $\cdot\text{OH}$  radicals involved in the photooxidation of the model compound in the presence of a synthesized catalyst. TA reacts with  $\cdot\text{OH}$  radicals to form a profoundly fluorescent 2-hydroxy terephthalic acid (TAOH) [37], and the fluorescence intensity is straightforwardly related to the convergence of  $\cdot\text{OH}$  generation, which responds with terephthalic acid to form fluorescent adduct in a specific reaction that is accountable for the PL signal. Figure S8b shows the increase in fluorescence intensity at various time intervals due to the formation of 2-hydroxy terephthalic acid (TAOH) upon irradiation of an alkali solution of TA in the presence of Fe@ZnS QDs/TiO<sub>2</sub> composite under a visible light source, demonstrating  $\cdot\text{OH}$  could also be a significant species for the degradation process. So as to comprehend the role of Fe@ZnS QDs/TiO<sub>2</sub> for the improved photocatalytic activity, a conceivable photodegradation mechanism is proposed on RhB, as shown in Fig. 9, and could be explained by the following steps:

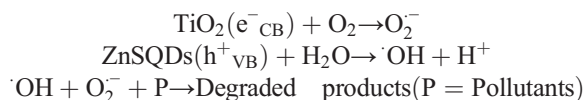
Step 1: Electron and hole pair generation



Step 2: Charge trapping



Step 3: Reduction-oxidation process



TiO<sub>2</sub> acts as an n-type semiconductor [38], while Fe@ZnS QDs act as a p-type semiconductor [39]. The bandgap energy of TiO<sub>2</sub> (P25) is 3.32 eV [40], equivalent to an absorption threshold of 373 nm. Along these lines, when Fe@ZnS QDs/TiO<sub>2</sub> are initiated under light illumination, both semiconductors are energized, and  $e^-$ - $h^+$  sets are produced in TiO<sub>2</sub> and in Fe@ZnS QDs. The electrons excited in the CB of Fe@ZnS QDs are moved to the CB of TiO<sub>2</sub>, and a huge number of the electrons are attained in the CB band of TiO<sub>2</sub> contrasted with TiO<sub>2</sub> alone. These electrons respond with O<sub>2</sub> to create O<sub>2</sub><sup>•-</sup> species. At the same time, the holes in the VB of TiO<sub>2</sub> are moved to the other way to the VB of Fe@ZnS QDs, which upon response with adsorbed water molecules, create  $\cdot\text{OH}$  as shown in Fig. 9. This successful parting of  $e^-$ - $h^+$  pairs in Fe@ZnS QDs/TiO<sub>2</sub> initiating from the p-n heterojunction

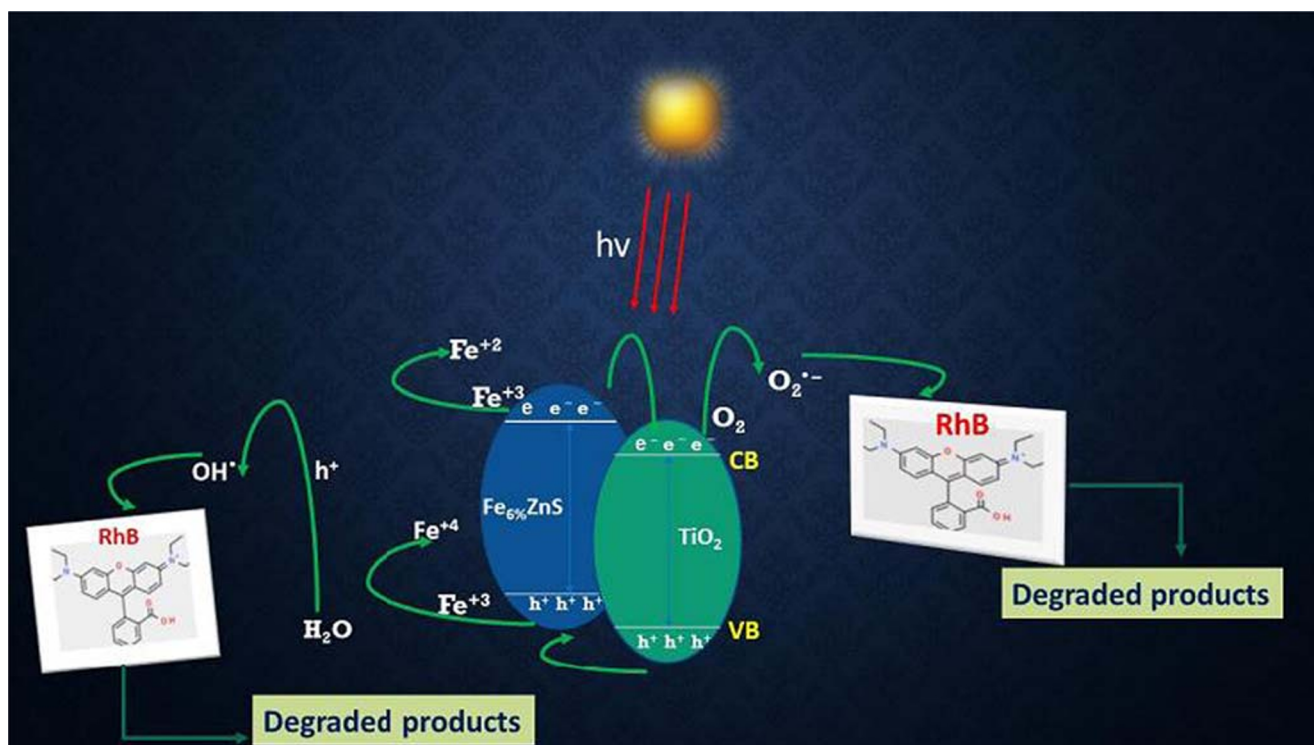


Fig. 9 Schematic diagram showing the possible photocatalytic mechanism of Fe@ZnS QDs/TiO<sub>2</sub> towards dye degradation

between TiO<sub>2</sub> and Fe@ZnSQDs is possibly responsible for the separation of charge carriers lifetime and, in this manner, the improved photocatalytic activity observed.

## 4 Conclusions

In summary, a profoundly active Fe@ZnSQDs/TiO<sub>2</sub> was successfully synthesized by precipitation method followed by their characterization using standard techniques such as XRD, FTIR, FESEM, EDX, UV–Visible, XPS, and PL studies. The photocatalytic activity of all nanocomposites has been explored by analyzing the degradation of two dissimilar chromophoric compounds both under UV- and visible-light sources. Additionally, Fe@ZnSQDs/TiO<sub>2</sub> indicated predominant activity on the way to the degradation of RhB and paracetamol because of its prolonged light absorption and minimized charge carriers. Furthermore, trapping experiments indicate superoxide radicals and hydroxyl radicals being the main receptive species associated with the degradation of organic pollutants. Based on the results, a conceivable photodegradation mechanism for the improved photocatalytic action of Fe@ZnSQDs/TiO<sub>2</sub> has been examined and proposed. In addition, the photoelectrochemical performance of as-prepared photocatalysts towards water oxidation was investigated in a three-electrode quartz cell assembly. The increasing order of photocurrent is discerned to be TiO<sub>2</sub> < ZnSQDs < Fe@ZnSQDs < Fe@ZnSQDs/TiO<sub>2</sub>. The highest photocurrent (approximately 0.12 mA cm<sup>-2</sup>) was recorded in the presence of Fe@ZnSQDs/TiO<sub>2</sub>, while the TiO<sub>2</sub> electrode produced the lowest photocurrent (0.02 mA cm<sup>-2</sup>). The current signal detected in the absence of light was negligible, suggesting the generated photocurrent is the result of photoexcitation.

**Acknowledgments** DST and UGC are appreciatively acknowledged for research support (DRS II, PURSE & FIST) to the Department of Chemistry, AMU Aligarh.

**Funding** The work is financially supported by the research project from the Science and Engineering Research Board, Government of India (CRG/2019/001370).

## Compliance with ethical standards

**Conflict of interest** The authors declare that they have no conflict of interest.

## References

- Alam N, Sarma D (2020) Tunable metallogels based on bifunctional ligands: precursor metallogels, spinel oxides, dye and CO<sub>2</sub> adsorption. *ACS Omega* 28:17356–17366
- Zeng J, Peng C, Wang X (2019) One-pot self-assembled TiO<sub>2</sub>/graphene/poly(acrylamide) super porous hybrid for photocatalytic degradation of organic pollutants. *J Appl Polym Sci* 136:47033
- Su D, Teoh CL, Samanta A (2015) The development of a highly photostable and chemically stable zwitterionic near-infrared dye for imaging applications. *Chem Commun* 51:3989–3992
- Neese F, Atanasov M, Bistoni G (2019) Chemistry and quantum mechanics in 2019: give us insight and numbers. *J Am Chem Soc* 141:2814–2824
- La Porta FA, Nogueira AE, Gracia L (2017) An experimental and theoretical investigation on the optical and photocatalytic properties of ZnS nanoparticles. *J Phys Chem Solids* 103:179–189
- Lashgari H, Boochani A, Shekaari A (2016) Electronic and optical properties of 2D graphene-like ZnS: DFT calculations. *Appl Surf Sci* 369:76–81
- Saikia D, Raland R, Borah JP (2016) Influence of Fe doping on the structural, optical and magnetic properties of ZnS diluted magnetic semiconductor. *Phys E Low-Dimensional Syst Nanostructures* 83: 56–63
- Rajabi HR, Khani O, Shamsipur M, Vatanpour V (2013) High-performance pure and Fe<sup>3+</sup>-ion doped ZnS quantum dots as green nano photocatalysts for the removal of malachite green under UV-light irradiation. *J Hazard Mater* 250–251:370–378
- Shamsipur M, Rajabi HR (2014) Study of photocatalytic activity of ZnS quantum dots as efficient nanoparticles for removal of methyl violet: effect of ferric ion doping. *Spectrochim Acta - Part A Mol Biomol Spectrosc* 122:260–267
- Kanemoto M, Hosokawa H, Wada Y (1996) Semiconductor photocatalysis: part 20. - role of surface in the photoreduction of carbon dioxide catalyzed by colloidal ZnS nanocrystallites in organic solvent. *J Chem Soc Faraday Trans* 92:2401–2411
- Torabi A, Staroverov VN (2015) Band gap reduction in ZnO and ZnS by creating layered ZnO/ZnS heterostructures. *J Phys Chem Lett* 6:2075–2080
- Umrao S, Abraham S, Theil F (2014) A possible mechanism for the emergence of an additional band gap due to a Ti-O-C bond in the TiO<sub>2</sub>-graphene hybrid system for enhanced photodegradation of methylene blue under visible light. *RSC Adv* 4:59890–59901
- Hu L, Chen F, Hu P (2016) Hydrothermal synthesis of SnO<sub>2</sub>/ZnS nanocomposite as a photocatalyst for degradation of Rhodamine B under simulated and natural sunlight. *J Mol Catal A Chem* 411: 203–213
- Zhang C, Zhou Y, Bao J (2018) Structure regulation of ZnS@g-C<sub>3</sub>N<sub>4</sub>/TiO<sub>2</sub> nanospheres for efficient photocatalytic H<sub>2</sub> production under visible-light irradiation. *Chem Eng J* 346:226–237
- Suyana P, Nishanth Kumar S, Madhavan N (2015) Reactive oxygen species (ROS) mediated enhanced anti-candidal activity of ZnS-ZnO nanocomposites with low inhibitory concentrations. *RSC Adv* 5:76718–76728
- Labiadh H, Ben CT, Balan L (2014) Preparation of Cu-doped ZnS QDs/TiO<sub>2</sub> nanocomposites with high photocatalytic activity. *Appl Catal B Environ* 144:29–35
- Wang YF, Zhang W (2014) Chemical depositing of CdS/ZnS composition nanostructure modified TiO<sub>2</sub> thin film. *Chalcogenide Lett* 11:389–395
- Velusubhash S, Kalirajan K, Harikengaram S (2018) Influence of co-dopant on structural, optical and electrochemical properties of zinc sulphide quantum dots. *J Nanosci Technol* 4:461–466
- Alam U, Khan A, Bahnemann D, Muneer M (2018) Synthesis of Co doped ZnWO<sub>4</sub> for simultaneous oxidation of RhB and reduction of Cr (VI) under UV-light irradiation. *J Environ Chem Eng* 6:4885–4898
- Khan A, Alam U, Raza W (2018) One-pot, self-assembled hydrothermal synthesis of 3D flower-like CuS/g-C<sub>3</sub>N<sub>4</sub> composite with enhanced photocatalytic activity under visible-light irradiation. *J Phys Chem Solids* 115:59–68

21. Alam U, Fleisch M, Kretschmer I (2017) One-step hydrothermal synthesis of Bi-TiO<sub>2</sub> nanotube/graphene composites: an efficient photocatalyst for spectacular degradation of organic pollutants under visible light irradiation. *Appl Catal B Environ* 218:758–769
22. Alam U, Khan A, Bahnemann D, Muneer M (2018) Synthesis of iron and copper cluster-grafted zinc oxide nanorod with enhanced visible-light-induced photocatalytic activity. *J Colloid Interface Sci* 509:68–72
23. Ji H, Fan Y, Yan J (2017) Construction of SnO<sub>2</sub>/graphene-like g-C<sub>3</sub>N<sub>4</sub> with enhanced visible light photocatalytic activity. *RSC Adv* 7:36101–36111
24. Raza W, Khan A, Alam U (2016) Facile fabrication of visible light induced Bi<sub>2</sub>O<sub>3</sub> nanorod using conventional heat treatment method. *J Mol Struct* 1107:39–46
25. Khan A, Alam U, Ali D, Muneer M (2018) Visible-light induced simultaneous oxidation of methyl orange and reduction of Cr(VI) with Fe(III)-grafted K<sub>2</sub>Ti<sub>6</sub>O<sub>13</sub> photocatalyst. *ChemistrySelect* 3: 7906–7912
26. Sofyan N, Ridhova A, Yuwono AH, Udhiarto A (2018) Preparation of anatase TiO<sub>2</sub> nanoparticles using low hydrothermal temperature for dye-sensitized solar cell. *IOP Conf Ser Mater Sci Eng* 316: 012055
27. Beranek R, Kisch H (2007) Tuning the optical and photoelectrochemical properties of surface-modified TiO<sub>2</sub>. *Photochem Photobiol Sci* 7:40–48
28. Baruah JM, Kalita S, Narayan J (2019) Green chemistry synthesis of biocompatible ZnS quantum dots (QDs): their application as potential thin films and antibacterial agent. *Int Nano Lett* 9:149–159
29. Fomichev VV, Kondratov OI (1994) Vibrational spectra of compounds with the wolframite structure. *Spectrochim Acta Part A Mol Spectrosc* 50:1113–1120
30. Liang YC, Wang CC (2018) Surface crystal feature-dependent photoactivity of ZnO-ZnS composite rods: via hydrothermal sulfidation. *RSC Adv* 8:5063–5070
31. Liu H, Yang W, Ma Y (2003) Synthesis and characterization of titania prepared by using a photoassisted sol-gel method. *Langmuir* 19:3001–3005
32. Santara B, Giri PK, Dhara S (2014) Oxygen vacancy-mediated enhanced ferromagnetism in undoped and Fe-doped TiO<sub>2</sub> nanoribbons. *J Phys D Appl Phys* 47:235304
33. Chithambararaj A, Sanjini NS, Bose AC, Velmathi S (2013) Flower-like hierarchical h-MoO<sub>3</sub>: new findings of efficient visible light driven nano photocatalyst for methylene blue degradation. *Catal Sci Technol* 3:1405–1414
34. Alam U, Kumar S, Bahnemann D (2018) Harvesting visible light with MoO<sub>3</sub> nanorods modified by Fe(III) nanoclusters for effective photocatalytic degradation of organic pollutants. *Phys Chem Chem Phys* 20:4538–4545
35. Lee J, Han CS (2014) Large-scale synthesis of highly emissive and photostable CuInS<sub>2</sub>/ZnS nanocrystals through hybrid flow reactor. *Nanoscale Res Lett* 9:1–8
36. Poornaprakash B, Amaranatha Reddy D, Murali G (2013) Composition dependent room temperature ferromagnetism and PL intensity of cobalt doped ZnS nanoparticles. *J Alloys Compd* 577:79–85
37. Khan A, Danish M, Alam U (2020) Facile synthesis of a Z-scheme ZnInS<sub>4</sub>/MoO<sub>3</sub> heterojunction with enhanced photocatalytic activity under visible light irradiation. *ACS Omega* 5:8188–8199
38. Sarkar D, Ghosh CK, Mukherjee S, Chattopadhyay KK (2013) Three dimensional Ag<sub>2</sub>O/TiO<sub>2</sub> type-II (p-n) nano heterojunctions for superior photocatalytic activity. *ACS Appl Mater Interfaces* 5: 331–337
39. Ortíz-Ramos DE, González LA, Ramirez-Bon R (2014) P-type transparent Cu doped ZnS thin films by the chemical bath deposition method. *Mater Lett* 124:267–270
40. Hagfeldt A, Grätzel M (1995) Light-induced redox reactions in nanocrystalline systems. *Chem Rev* 95:49–68

**Publisher's note** Springer Nature remains neutral with regard to jurisdictional claims in published maps and institutional affiliations.